CARBON-CHAIN MOLECULES IN LOW-MASS PROTOSTELLAR SYSTEMS L1489 AND L1527

LISA POTHOVEN

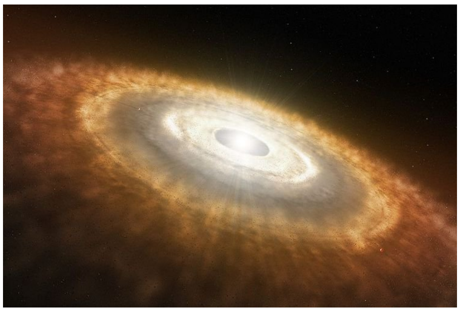

First Master Project

Astronomy
Faculty of Science
Leiden University

31 July 2019

Lisa Pothoven: *Carbon-Chain Molecules in Low-Mass Protostellar Systems L1489 and L1527*, Submitted for the First MSc Research Project in Astronomy.

SUPERVISORS:
Dr. Michiel Hogerheijde
Dr. Daniel Harsono

LOCATION:
Leiden

TIME FRAME:
20 September 2018 - 31 July 2019

Cover page image credit: ESO/L. Calçada.

ABSTRACT

Molecular clouds are cold (~ 10 K), dark regions, in which star formation takes place. The stages that a protostar and its surrounding disk and envelope go through in their lifetime before becoming a main-sequence star and forming planetary system, determine the physical conditions and chemical diversity in the system. Carbon-Chain (CC) molecules are known to be less abundant around young stars, and are therefore more difficult to observe in detail. Radio interferometry presents possibilities of high resolution spectroscopy (on spatial as well as spectral scale). In this report we present our study of the presence of CC-molecules in the young protostellar systems L1489 IRS and L1527 IRS. We have found that C_4H, C_6H, l-C_3H_2, c-C_3H_2, and HC_3N are detected toward L1527, and that C_4H is detected toward L1489. A few lines of l-C_3H_2, and c-C_3H_2 are observed toward L1489, but are considered doubtful. We conclude that the difference in CC-molecule abundance between these sources is most likely explained by the difference in stellar mass and envelope mass. L1527 is in the early Class 0 stage, heavily accumulating material onto the disk and star. Whereas L1489, classified as a Class I protostar, seems to be more mature, with almost no envelope material left and less CC-chemistry occurring. The presence of C_4H in L1489 is remarkable in this stage of the star formation process. It gives rise to the question if new C_4H molecules are being formed, or whether it is a remnant of previous reactions.

ACKNOWLEDGEMENTS

I would like to thank Michiel Hogerheijde and Daniel Harsono for their guidance throughout the various stages of this research project, and for their understanding and support in the more difficult moments.

CONTENTS

LIST OF FIGURES

ACRONYMS

1 INTRODUCTION

1.1 LOW-MASS YOUNG STELLAR OBJECTS

Molecular clouds are sites of star formation. A molecular cloud is a cold ($T_K \sim 10$ K), higher density ($n > 30$ cm^{-3}) region in the Interstellar Matter (ISM) [13]. They are mainly heated by cosmic rays and the interstellar radiation field. Within a molecular cloud, globules and cores form. A prestellar core is a dense region within the cloud which can become gravitationally bound, and eventually collapse [13]. When this happens, material from the surrounding bulk, referred to as the envelope (usually with a radius of the order $\sim 10^3$ AU), starts to accrete and form a protostar. Leftover rotation leads to flattening of the envelope and eventually forms a rotationally supported disk. Magnetic fields together with rotation lead to winds and jets, resulting in molecular outflows [13] in order to conserve the angular momentum. This process happens gradually and can be divided into evolutionary phases. A Young Stellar Object (YSO) starts off with more mass in the envelope than in the star and disk together. Gradually, it will evolve into a system where most mass is in the star (in $\sim 10^5$ year) [13]. Globules and cores come in a range of sizes and masses. The ones that we are able to observe are probably at the low end of the general distribution of cloud sizes. The inner part (about 100 AU or less) of a YSO is heated by the protostar to temperatures of about 100 K. These inner regions can contain complex molecules [8]. Usually, species with six or more atoms are considered complex [8]. Examples of complex molecules are radicals with the C_nH structure, cyanopolyynes (HC_nN) and isomers thereof, and molecules containing uncommon isotopes such as deuterium (D). Carbon is the most common element in all of these molecules [8].

The origin of this chemical diversity may lie in the duration of the evolutionary phases that a protostar undergoes in its lifetime. For example, a low mass ($\sim 2M_\odot$) star forms within 10^6 year, while higher mass stars form in $< 10^5$ year. The onset of star formation can be explained by a fairly simple model of gravitational collapse. The length of the evolutionary phases, together with the conditions in the cloud, regulates the growth and mass distribution of the young star and its protoplanetary disk. This formation process can be studied in, sometimes isolated, low-mass stars in nearby clouds [13].

Figure 1: The inside-out collapse of a molecular cloud begins in the center. The radius at which matter falls inward keeps expanding as the outer parts lose their pressure support.

1.2 THE COLLAPSE OF MOLECULAR CLOUDS

The first phase of star formation is the collapse of a molecular cloud. This is followed by the accretion of material from the outer envelope onto the central star, accompanied by the formation of a disk around the star. The density of a star is generally twenty orders of magnitude greater than that of the cloud, the temperature is about six orders of magnitude higher. This change in density and temperature requires an instability (i.e. a supernova), leading to the collapse of the cloud. In the following paragraphs, we will take a look at the different ways of collapse.

1.2.1 *Inside-out collapse*

In the case of inside-out collapse, the disruption begins in the center, where the density is highest. Matter inside a radius $r_{inf} = at$ falls inwards after a time t. This free-fall time decreases towards the center ($t_{ff} \sim \rho^{-1/2}$). Therefore the central parts of the sphere collapse faster than the outer parts. As the surrounding parts lose their pressure support, the wave of collapse travels outwards at the speed of sound [20]. See figure 1[1].

The inside-out collapse consists of four phases. (1 - Free-fall) The cloud collapses at a free-fall timescale, (2 - First core) the first stable core forms, it is a few AU in size, (3 - Opacity) the opacity of the cloud increases (first in the infra-red (IR) regime), and (4 - Accretion) the protoplanetary disk starts to form and the protostar becomes visible in the IR.

1.2.2 *Thermal support*

Inside-out collapse is a simplified description of how a cloud collapses. However, regular free-fall collapse would lead to thirty times the average star forming rate in the Milky Way [13]. Something must support these clouds against collapse. The basic form of support is

1 Image taken from https://staff.fnwi.uva.nl/c.dominik/Teaching/SPF/04-collapse.pdf

thermal support. In this case, collapse can only occur when $M_{cloud} > M_J$. Where M_J is the Jeans mass.

$$M_J = \left(\frac{\pi k T_K}{\mu m_H G}\right)^{1.5} \rho^{-0.5} = 18\ M_\odot T_K^{1.5} n^{-0.5}$$

Here, T_K (K) is the kinetic temperature, ρ (g cm^{-3}) is the mass density, n (cm^{-3}) is the particle density [21].

1.2.2.1 *Magnetic field*

Thermal support does not provide a complete explanation of cloud support. Another contribution is the magnetic field of the YSO. This magnetic field provides support against the cloud collapse by restricting ionized particles to move along the lines of the field. This process allows neutral gas to move across field lines in a timescale of $t_{AD} \approx 7.3 \times 10^{13} x_e$ years, where x_e is the ionization fraction. Once the cloud collapses, a magnetic field helps material flow into a pseudodisk at a scale of ~ 1000 AU. This might explain larger, flattened structures [13].

1.2.2.2 *Turbulence*

Most molecular clouds undergo turbulence. This means that observed molecular lines become wider or narrower due to local motions in the cloud. Information on the velocity distribution ($\vec{v}(\vec{r})$) is obtained by creating a map of line profiles over the area of a molecular cloud [6]. Motions along the line of sight produce Doppler shifts. Line width can also increase due to thermal broadening. The line width is larger for larger clouds, according to the line-width-size relation: $\Delta v \propto R^\gamma$ [15].

1.2.2.3 *Rotation*

Initially, a cloud rotates slowly as a solid body. Rotation is able to support clouds against the early stage of collapse, except along the rotation axis. At that point, the outer envelope stays spherical, while the inner region starts distorting into a flattened disk-like structure. Eventually, rotation will not prevent collapse anymore, and will even be amplified in later phases. See figure 2 [13].

Within the cloud, parcels of gas are rotating around the center at a specific angular momentum. The gas will accrete onto the disk at a radius corresponding to their angular momentum.

A disk supported by rotation, should have a characteristic radius of

$$r_c = \frac{G^3 M^3 \Omega^2}{16 a^8}$$

where M is the mass of the (proto)star and disk.

Figure 2: Sketch of the inside-out collapse including rotation.

1.2.3 *Collapse indicators*

Radio interferometers such as Atacama Large Millimeter/submillimeter Array (ALMA) allow for high spectral resolution spectroscopy on a spatial scale. This offers the possibility to search for molecular lines within the emission of an extended object. The high angular resolution of ALMA makes it possible to determine exactly where emission is coming from [11].

The typical indication of an inside-out collapse is a double peaked molecular line. This signature is a result of the infall motion of regions around the protostar. Regions behind the star (on the line of sight) will be blueshifted, while a regions in front of the star will be redshifted. The blue peak is usually higher than the red peak [6], since some of the cooler material absorbs radiation from hotter regions. In order for the difference between these two peaks to occur, the two corresponding regions should lie along an optically thick line of sight (for the frequency that corresponds to the molecular line). Optically thin material does not absorb any radiation, and thus the profile stays symmetric [6]. See figure 3[2] for a visual reference.

An asymmetric line profile does not always indicate a collapsing core. A collapsing core must also show an optically thin line that peaks between the two peaks of the opaque line. The reason for this is that there are other objects, such as colliding fragments, that could produce a double-peaked profile. These would also produce this profile in an optically thin line. An optically thin line does not absorb radiation and therefore should form only a single peak in the spectrum of a collapsing core [6].

1.2.4 *Gas physical conditions*

Important physical conditions of the gas in a molecular cloud are: kinetic temperature (T_K), particle density (n), velocity ($\vec{v}$), magnetic field ($\vec{B}$), and ionization fraction (Ξ). From these conditions, we can calculate the column density,

$$N \equiv \int n dl,$$

and the cloud mass

$$M_N \equiv \int N da.$$

2 Image taken from https://staff.fnwi.uva.nl/c.dominik/Teaching/SPF/04-collapse.pdf

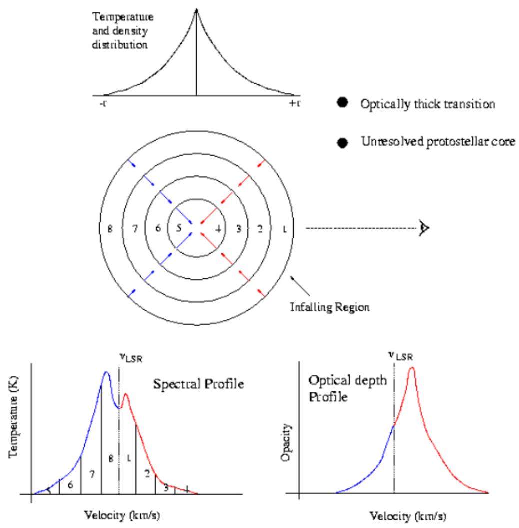

Figure 3: The formation of the asymmetric line profile in a collapsing core.

1.2.4.1 *Dust physical conditions*

Physical conditions for the dust in a molecular cloud are: dust temperature (T_D), dust grain density (n_D), opacity at given frequency ($\kappa(\nu)$), and optical depth ($\tau_D(\nu) = \kappa(\nu)N$).

1.2.5 *Continuum emission*

Continuum radiation can be studied at low spectral resolution. It is helpful in reconstructing the total luminosity and mass of envelopes, protostars and disks. A comparison of these masses provides information on the evolutionary status of star- and planet formation [14]. It tells us what fraction of the initial mass has been accreted onto the star, what fraction is being carried away by outflow and what has ended up in a disk [12]. The energy distribution of early stage YSOs can be approximated by a single temperature black-body. In later stages, the stellar black-body peaks in the optical regime, and the protoplanetary disk in the infrared.

Dust in a protostellar core is approximated to be optically thin and isothermal with a temperature of 10 to 15 K [12]. Dust mass is determined by measurements of the column density and temperature. The intensity profile can be found by integrating the temperature and density profile along the line of sight [22]. However, both temperature and density vary throughout disks and envelopes. Due to the protostar, which acts an internal heating source, the envelope has a luminosity-dependent temperature distribution [12]. There are large continuum surveys available for disentangling the envelope and disk contributions from the dust continuum emission ([12]).

1.2.6 *Line emission*

After determining the mass of the disk and the envelope, another component of the YSO remains; the protostar. Spectrally as well as spatially resolved line observations provide a look into the structure of the inner envelope and disk. This gives rise to a derivation of the stellar mass [12].

HCO+ and HCN lines are good tracers of motions in the inner envelopes and disks. HCO^+ 3-2 emission is used to detect Keplerian rotation. The mass of the star is derived by creating a position-velocity curve from the position of the peak emission, projected on the major axis of the HCO^+ emission [12]. A Keplerian rotation curve is then fitted to this curve, with the systemic velocity and central mass as free parameters.

Future ALMA observations will provide the spectral sensitivity to observe molecules that are less abundant. By observing less prominent line profiles, more can be learned about the gas motion inside the YSO.

1.2.7 *Disk formation*

1.2.7.1 *The luminosity problem*

Observations of YSOs show that they are less luminous than their expected luminosity, based on constant mass accretion onto the central star. This would suggest that the material is accreted onto the protostar indirectly, for example through a circumstellar disk, which lowers the amount of released gravitational energy [12].

Material infalling from the outer core is deflected from the central star into a disk at the centrifugal radius, where gravity is balanced by rotation. The centrifugal radius will grow in time. Disk formation might occur in episodic events [12].

1.3 CLASSIFICATION

YSOs can be classified according to different properties. Their bolometric temperature is a general indicator of their evolutionary stage. The protostellar phase for low-mass stars lasts about 10^5 years [3]. In this phase, the mass of the star, circumstellar disk, and the chemical composition of the disk are determined [3].

Class 0

When the cloud has just begun its collapse, it is classified as Class 0. These objects are deeply embedded in their surrounding envelopes. Since the protostar and the disk around it are very young, the envelope still contains more than half of the total mass [11]. A common envelope mass is $\sim 0.5 M_{\odot}$. The disk-to-envelope mass ratio is about 1 to 10% [12]. The duration of the Class 0 phase is ~ 0.1 Myr. Emission is most visible in the far-infrared and sub-millimeter. $T_{bol} < 70K$. Due to the angular momentum of the cloud, which is causing the formation of a dense disk, most YSOs undergo a material outflow along their rotational axis (bipolar outflow) [4].

Class I

Class I sources are similar to Class 0, but the disk-to-envelope mass ratio has increased to 20-60 % [12]. The bolometric temperature is $70 < T_{bol} < 650K$ and the duration of the phase is ~ 0.44 Myr. 87% of the observed continuum flux comes from the disk, as opposed to 68% for Class 0 [12].

Class II

The bipolar outflows have dispersed most of the envelope. The pre-main sequence star will be revealed. The density of the disk around the star now allows for the formation of pebbles, rocks and planetesimals, and eventually leads to planet formation. The temperature is $650 < T_{bol} < 2800K$, and the phase duration is 2 ± 1 Myr. Most of the emission is visible in the near-infrared.

Class III

In the end, most of the material has accreted at the pre-main-sequence star. There is little or no disk left between the planetesimals. It is possible that planets have formed.

See figure 4 for an overview of pre- and protostellar object structure [3].

1.4 CHEMISTRY

During star- and planet formation, molecules in molecular clouds change largely in abundance. The gas, ice and dust undergo a variety of chemical transformations in response to large changes in physical conditions. Temperatures vary from 10 K to 1000 K, densities from $\sim 10^4$ to more than 10^{10} H_2 molecules cm^{-3}. In the cold protostellar phase, most molecules are frozen. As the protostar begins to heat up, ice evaporates and complex molecules start to form. Heavy UV and X-ray radiation impacts the molecules further by photo-dissociation, -ionization and -desorption [4], [3].

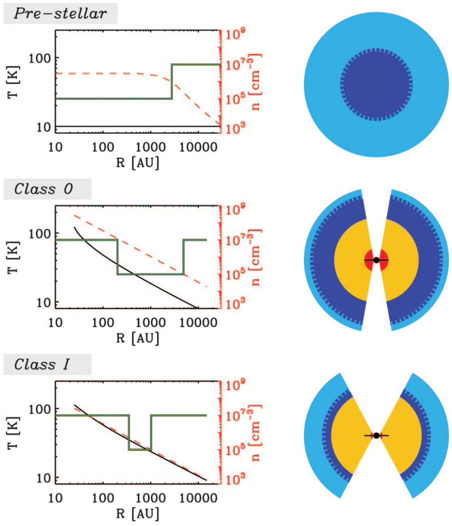

Figure 4: Physical and chemical structure of protostellar objects. Dark blue indicates freeze-out areas (light blue areas have too low density for freeze-out), in yellow regions CO ice evaporation takes place, and in red regions H_2O ice evaporation. Image from Van Dishoeck (2006) [3].

1.4.1 *Molecular gas*

The most abundant molecule in the gas in a molecular cloud is H_2 [13]. However, the low mass of this molecule means that it requires quite high excitation temperatures for rotational transitions. A molecule like CO has stronger lines and is therefore easier to observe. The luminosity of CO (J=1-0) can be used to measure cloud mass [13].

1.4.2 *Protostellar Envelopes*

Interactions between gas and solids are important for the chemistry in star-forming regions. H_2O is expected to form on the grains. Radiation emitted by the young star can ionize or dissociate molecules in the inner envelope.

1.4.3 *Protoplanetary Disks*

The basic chemical structure of a disk consists of three layers [5]. The layer closest to the star is the photon-dominated region, where molecules are photo-dissociated and atoms ionized by UV radiation. After that comes the warm molecular (intermediate) layer, where molecules are subjected to moderate radiation, and high enough temperatures to prevent freeze-out. This is where active chemistry occurs. At the edges follows the cold midplain, where molecules are frozen and no reactions take place. Various ices have different sublimation temperatures. Species come off the grains at different radii. Once the ices evaporate, complex molecules can form. Within the disk, the densities, temperatures and radiation are much higher than in the envelope. The chemistry in the second layer is influenced by grain growth and grain settling. The available grain surface area influences the rate of molecule formation.

1.5 CARBON-CHAIN MOLECULES

Carbon-chain molecules are common in the early stage of the evolution of a YSO [19]. CC molecules are an important source of organic material in molecular clouds. It is expected that these molecules will end up in protoplanetary disks, and eventually in planets. The presence of CC molecules is expected to recede once a protostar is formed and most carbon atoms have been captured as CO [16].

Massive stars are relatively easier targets to observe their chemical complexity. It is more difficult to study low-mass systems, but recent studies show promising results of complex molecules in protostellar regions [11]. What is still unknown, is the degree of chemical complexity that a low-mass protostar can reach, how and where complex molecules form, in what way reactions take place, and what external factors might play a role [11].

1.6 OUTLINE

In this report we will take a look at protostellar sources L1489 IRS and L1527 IRS. Using data from ALMA we study the presence of CC molecules in and around these protostars. First, we will describe the sources themselves, give background information on ALMA. Then, we go into the steps taken in the process of identifying the CC molecules. After this, we present which CC molecules we were able to detect, along with other interesting data. Finally, we conclude with what we can learn about the physical and chemical structure of L1489 IRS and L1527 IRS from these results.

2 OBSERVING TARGETS AND DATA

2.1 OBSERVING TARGETS

Protostars L1489 IRS and L1527 IRS are both located in the Taurus Molecular Cloud at a distance of 140 pc (456.6 ly) [19]. They are in different phases of star and planet formation, which we will explain below.

2.1.1 *L1489*

L1489 IRS, with central protostar IRAS PSC 04016+2610, (α_{2000} = $04^h04^m43.1^s$, δ_{2000} $+26°18'56.4''$), is a class I Young Stellar Object (YSO) [12]. There is a faint molecular outflow in the north-south direction [25]. It is surrounded by a compact envelope which has a radius of 2000 AU [2]. The source is classified as class I, but it was hypothesized by Hogerheijde (2001) [9] that L1489 might be transitioning between a collapsing envelope and a Keplerian disk. The protostar has a bolometric luminosity of $L_{bol} = 3.70 L_\odot$ [10], stellar mass $M_* = 1.3 \pm 0.4 M_\odot$ [2] and surrounded by an envelope with $M_{env} = 0.11 M_\odot$ and a disk with $M_{disk} = 0.018 M_\odot$. The inclination is 74°. The systemic velocity is $v_{LSR} = 7.2$ km/s [2]. There is a nearby starless core at a 8400 AU distance.

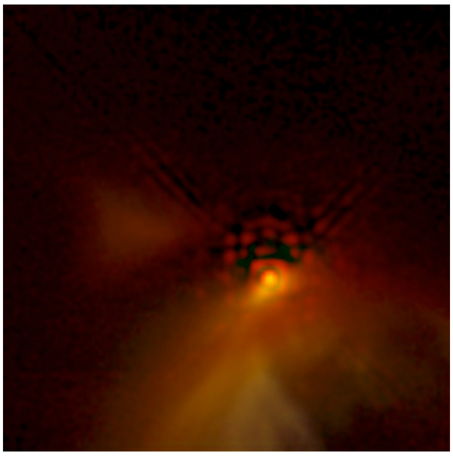

Figure 5: An image of L1489 and the surrounding envelope. The protostar is visible as an orange dot. *Credit: D. Padgett (IPAC/Caltech), W. Brandner (IPAC), K. Stapelfeldt (JPL) and NASA/ESA*

2.1.2 *L1527*

L1527 IRS, with central protostar IRAS 04368+2557 ($\alpha_{2000} = 04^h39^m53.89^s$, $\delta_{2000} = +26°03'11.0"$), is a Class 0 object [1]. The source seems to have a bipolar outflow of 2.0×10^4 yr old. Since the outflow is almost in the plane of the sky, the protostellar disk is viewed edge-on [19]. The envelope surrounding L1527 is estimated to have a 1000 AU radius [17]. The bolometric luminosity of the star is $L_{bol} = 1.30 L_\odot$, $M_{env} = 0.56 M_\odot$, $M_{disk} = 0.029 M_\odot$ [12]. The systemic velocity is 5.85 km/s [18]. The protostar in L1527 contains about 20% of the envelope mass. The disk is 180 AU in diameter. It is a young system, approximately 300,000 years old [23].

Figure 6: Protostar L1527 and the obscuring disk in the north-south direction. Image taken from [23].

2.2 ALMA

The Atacama Large Millimeter/submillimeter Array (ALMA) is composed of 66 antennas located in the Chilean Andes at an elevation of 5000 m and a latitude of $-23°$. Observations for our data were carried out using two ALMA configurations. The Atacama Compact Array (ACA) antennas, with 12 antennas of 7m in diameter, and a primary beam of $\sim 35" \times 300/\nu$ GHz. The ACA's longest baseline is 50m. The second configuration is the Twelve Meter Array (TM), with 50 antennas that are 12m in diameter, a primary beam of $\sim 20.6" \times 300/\nu$ GHz and, in this case, a longest baseline of 400m. The ACA observations are meant for looking at large-scale structures, since the maximum baseline length is shorter and the antennas are closer together. The TM is used to detect small-scale structures. It is important to note that the observed peak intensities mentioned in this report are not integrated over the beam size of the arrays, and can therefore not be directly

Band	Spectral Window	ν_{min} (GHz)	ν_{max} (GHz)	ν_{central} (GHz)
3	2	104.801	105.729	105.291
3	3	104.001	104.929	104.491
4	2	142.504	144.311	143.328
4	4	153.061	154.877	153.999

Table 1: The ALMA bands, spectral windows, and the corresponding frequency ranges for the TM data, the central frequencies are only slightly different for the ACA data. Channel width is 255 kHz.

compared to each other.

ALMA offers multiple bands to carry out observations. The ALMA bands that were used for our research are listed in table 1. The channel width is 244 kHz. The number of ACA antennas is 10. L1489 was observed with ACA on 10-Oct-2016 from 08:12:15.1 to 08:46:37.9 UTC, and with TM on 21-Dec-2016 from 02:55:19.9 to 03:17:22.9 UTC. The longest ACA baseline is 48 m. The longest TM baseline is 500 m. L1527 was observed with ACA on 10-Oct-2016 from 08:08:55.2 to 08:42:43.8 UTC, and with TM on 21-Dec-2016 from 02:51:25.2 to 03:15:47.5 UTC.

3 METHODS

The data obtained from the observations has directly been imaged, we will not go into that process here. In this chapter we describe the process of line detection and identification.

3.1 CC-MOLECULES

The carbon-chain molecules that we are trying to find in L1527 and L1489 are: C_4H, C_6H, c-C_3H_2, l-C_3H_2, HC_3N and HC_5N. For transitions of these molecules, we notate the quantum numbers in this report as follows: (N J F - N J F), unless mentioned otherwise.

3.2 REGIONS

In order to study the spatial distribution of the molecules, we selected a range of different sized regions across the source. Region size (L), given in arcsec, is the maximum projected region on the source. These regions extend radially from the central pixel in the image, which corresponds to the center of the Point Spread Function (PSF). The region sizes were chosen as follows: 0": the PSF peak position, 5": the continuum source size, 15": the ACA beam size, and 30": further extended emission. The edges of the clouds are uncertain, so the largest region (30 arcsec) might not perfectly correspond to the cloud size.

3.3 FREQUENCY SHIFTS

Emission from both sources is influenced by different types of relative motion. The motion of the Earth around the Sun affects the amount of Doppler shift that radiation undergoes before reaching the detector surface. The operating frequency of the telescope (the sky frequency) needs to be corrected for the rotation of the Earth (0.5 km/s), the Earth and Moon center of mass orbit (0.013 km/s), the Earth orbital motion (up to 30 km/s), and the Local Standard of Rest (LSR) (20 km/s). Even though our images were calibrated, there was still a remaining frequency shift between the bands and telescope arrays of 0.01 to 0.02 GHz. These shifts result from different observing schedules for each band and array. This problem was solved by aligning a number of bright lines in the spectrum, which have a known, well-defined position.

In chapter 4 we will go further into the alignment of the spectra.

3.4 LINE DETECTION

To start, we looked at the raw data in CASA [1]. CASA is a radio astronomy software package meant for post-processing data from radio astronomical telescopes such as ALMA. It can be used to examine the data, the configuration of the antennas, and all the necessary details of the observation itself. The data was then transferred per spectral window to a plot of intensity in Kelvin and frequency in GHz. This was exported and saved for use in other software, in this case CASSIS [2]. CASSIS is a software package used to analyze spectra, compare with molecular databases, identify molecular lines, and create detailed fits of a spectrum.

The first step in the detection of the lines was to analyze the spectra by eye to find differences and similarities. This gives an indication of the brightest lines and how they compare the sources. For each spectral window, the rms value of the noise was calculated (more details in chapter 4). A significant line detection should have an intensity higher than 3σ. A list of all noise values for the different spectral windows can be found in table 3. After this, we went through the Carbon-Chain (CC) molecules on a line-by-line basis.

Altough we specifically look at carbon-chain molecules, other molecules should not be ignored since they can exclude false detections for the CC-molecules.

In CASSIS, we created a template of CC-molecules with species from the molecular databases JPL [3] and CDMS [4]. The lines that were detected by comparing the graphs of both sources, were checked in CASSIS for their precise positions and if corresponding transitions could be detected. A simple Gaussian fit was done in CASSIS, using the AMOEBA fitter, to retrieve information on the peak intensity and the line width.

1 *Common Astronomy Software Applications* `casa.nrao.edu`
2 `cassis.irap.omp.eu`
3 `spec.jpl.nasa.gov`
4 `cdms.astro.uni-koeln.de`

4 RESULTS

In this chapter, we present the results of the data analysis. First we show the final alignment of the two different bands. Then, we go through the detected CC molecules. For each CC molecule, we compare detected lines between L1527 and L1489, and between ACA and TM. We also look at the line width and intensity as functions of region size.

Figure 7 and 8 show the whole spectrum for both sources, using only the data from the ACA array.

4.1 SPECTRUM ALIGNMENT

The spectra for both sources were aligned using the following bright lines.

- c-C_3HD at $\nu_0 = 104187.108$ MHz, $E_{up} = 10.85$ K
- C_4H at $\nu_0 = 104705.11$ MHz, $E_{up} = 30.16$ K
- DCO^+ at $\nu_0 = 144077.214$ MHz, $E_{up} = 10.37$ K.

Both c-C_3HD and C_4H indicate a shift of $\Delta\nu = 5$ MHz for the ACA spectra, and $\Delta\nu = 6.8$ MHz for the TM spectra. DCO^+ shows that band 4 is shifted with $\Delta\nu_{TM} = 19.8$ MHz, $\Delta\nu_{ACA} = 4.6$ MHz. The final frequency shifts are listed in table 2.

c-C_3HD was only detected in L1527. A second, weaker transition ($\nu_0 = 104799.689$ MHz) is not convincingly present in our data, there are only minor (below the 3σ noise level) peaks visible (TM: $3\sigma = 0.985$K, ACA: $3\sigma = 0.035$K, table 3). See figure 16. Note that c-C_2HD has no lines above the noise level for L1489. Another candidate for this line would be sodium chloride (NaCl) (8 - 7). NaCl has been detected in the disk surrounding Orion Source I [7]. However, the line is very bright in L1527, and is more likely to be caused by c-C_3HD, which has the lowest E_{up} of the two.

4.2 DETECTION OF CC-MOLECULES

We will now go through the molecular lines that were found. We have detected five species, with a total of 23 lines, out of the six species of CC-molecules that we searched for in L1527 and L1489 (C_4H, C_6H, c-C_3H_2, l-C_3H_2, HC_3N and HC_5N). HC_5N was not detected.

Array	Band	SPW	Δν (MHz)
ACA	3	2	-5.0
		3	-5.0
	4	2	-3.9
		4	-4.4
TM	3	2	+6.4
		3	+6.4
	4	2	+20
		4	+19

Table 2: The frequency shifts applied to the data to correct for differences caused by the orbital movement of the Earth.

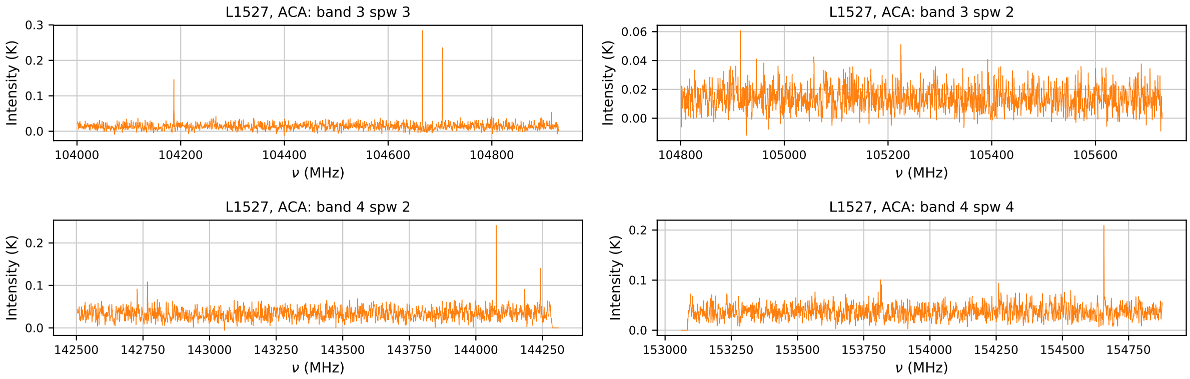

Figure 7: The complete spectrum (ACA data) of L1527 that was used in this research.

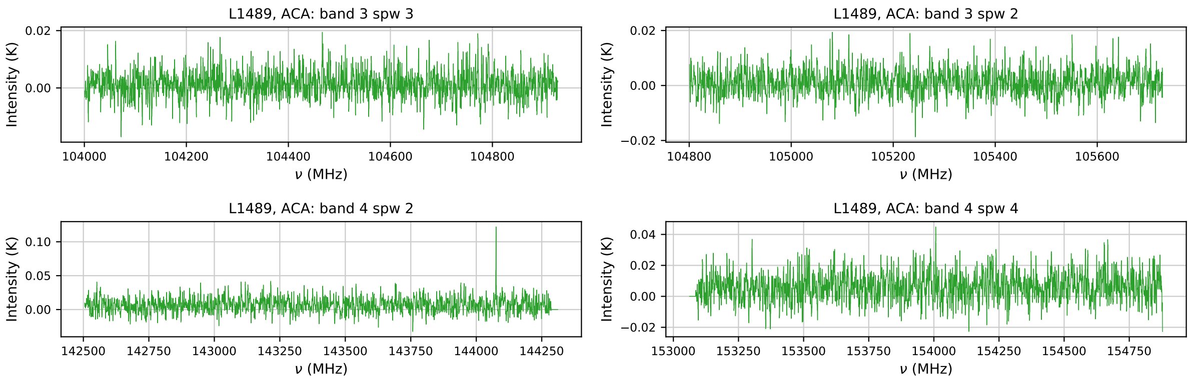

Figure 8: The complete spectrum (ACA data) of L1489 that was used in this research.

Tables 5 to 8 list the detected transitions for the CC-molecules. We made note of the frequency (and other transition parameters), velocity, peak intensity and line width. In some cases no lines are visible above the 3σ noise level and upper limits are given, a complete overview of all noise levels can be found in table 3. The lines are ordered by E_{up} per species. We will now go through each molecule in the table and compare the peak intensities and velocities of the lines in both sources and data sets

C_4H

We first detected the C_4H lines with the lowest upper state energy levels. These are (N=11-10, J=10.5-9.5, F=10-9) (E_{up} = 30.16 K) and (N=11-10, J=11.5-10.5, F=11-10) (E_{up} = 30.14 K). The peak intensities for L1527 are 1.09 ± 0.04K for the TM data, and 240 ± 7mK for the ACA data. C_4H also appears in the spectrum of L1489, but with a different transition as the strongest peak. This can be seen in figure 9. Peak intensities for L1489 are 249 ± 50mK for TM and < 13mK (below the 3σ noise level) for ACA data.

C_4H is easily detected in L1527 due to its relatively bright lines. The strongest lines of C_4H are found around 104.7 GHz and are clearly visible as a pair of bright lines (see figure 9). The pattern of these lines returns in both sources and for both telescope configurations. Not all other transitions could be identified, due to the high noise level. The ACA data for L1489 lacks the most transitions, compared to the rest of the data. Figure 10 shows that the C_4H emission extends over the entire 30" region, but is strongest toward the center. The intensity of C_4H peaks towards the central protostar for both sources.

C_6H

C_6H was only detected towards L1527 in the TM data. Two of the higher-excitation transitions have been detected (56 - 55, and hyperfine levels), but not the lower transitions. For the lower transitions, we sometimes find very weak lines, below the 3σ noise level (< 0.64 K for band 4, < 1.0 K for band 3). For example, a line with a peak intensity of 0.91K is found for L1527 (TM data) at $\nu_0 = 104716.548$MHz, N = 38-37. The intensities for the detected transitions are around 0.64K.

c-C_3H_2

c-C_3H_2 is detected towards both sources, but not all transitions are above the 3σ noise level. In L1527, the lowest three transitions (N=3-3, N=8-8, N=11-11) have been detected in the TM data. Although the first one is just below the 3σ noise level (< 0.64 K). The peak intensity in L1527 seems to be around 1K (TM data). Two c-C_3H_2 lines have a velocity higher than expected from the systemic velocity. These are the (N,J,F=8,8,1-8,7,2) and (N,J,F=12,6,7-11,9,2) transitions. For L1489, only two transitions have been detected. We also observe a peak at

Table 3: The 3 rms noise values for L1489 and L1527 for all bands, spectral windows and region sizes.

L1527					L1489				
Source	Band	Spw	Region (")	3σ (K)	Source	Band	Spw	Region (")	3σ (K)
ACA	3	2	0	0.032	ACA	3	2	0	0.013
			5	0.032				5	0.014
			15	0.025				15	0.011
			30	0.014				30	0.007
	3	3	0	0.035		3	2	0	0.013
			5	0.035				5	0.012
			15	0.028				15	0.011
			30	0.015				30	0.006
	4	2	0	0.068		4	2	0	0.036
			5	0.064				5	0.033
			15	0.041				15	0.023
			30	0.016				30	0.011
	4	4	0	0.074		4	4	0	0.031
			5	0.069				5	0.030
			15	0.041				15	0.018
			30	0.014				30	0.008
TM	3	2	0	1.016	TM	3	2	0	0.248
			5	0.274				5	0.099
			15	0.045				15	0.025
			30	0.017				30	0.010
	3	3	0	0.985		3	3	0	0.257
			5	0.271				5	0.100
			15	0.046				15	0.028
			30	0.018				30	0.010
	4	2	0	0.552		4	2	0	0.132
			5	0.198				5	0.074
			15	0.040				15	0.019
			30	0.010				30	0.005
	4	4	0	0.637		4	4	0	0.151
			5	0.210				5	0.078
			15	0.043				15	0.018
			30	0.010				30	0.004

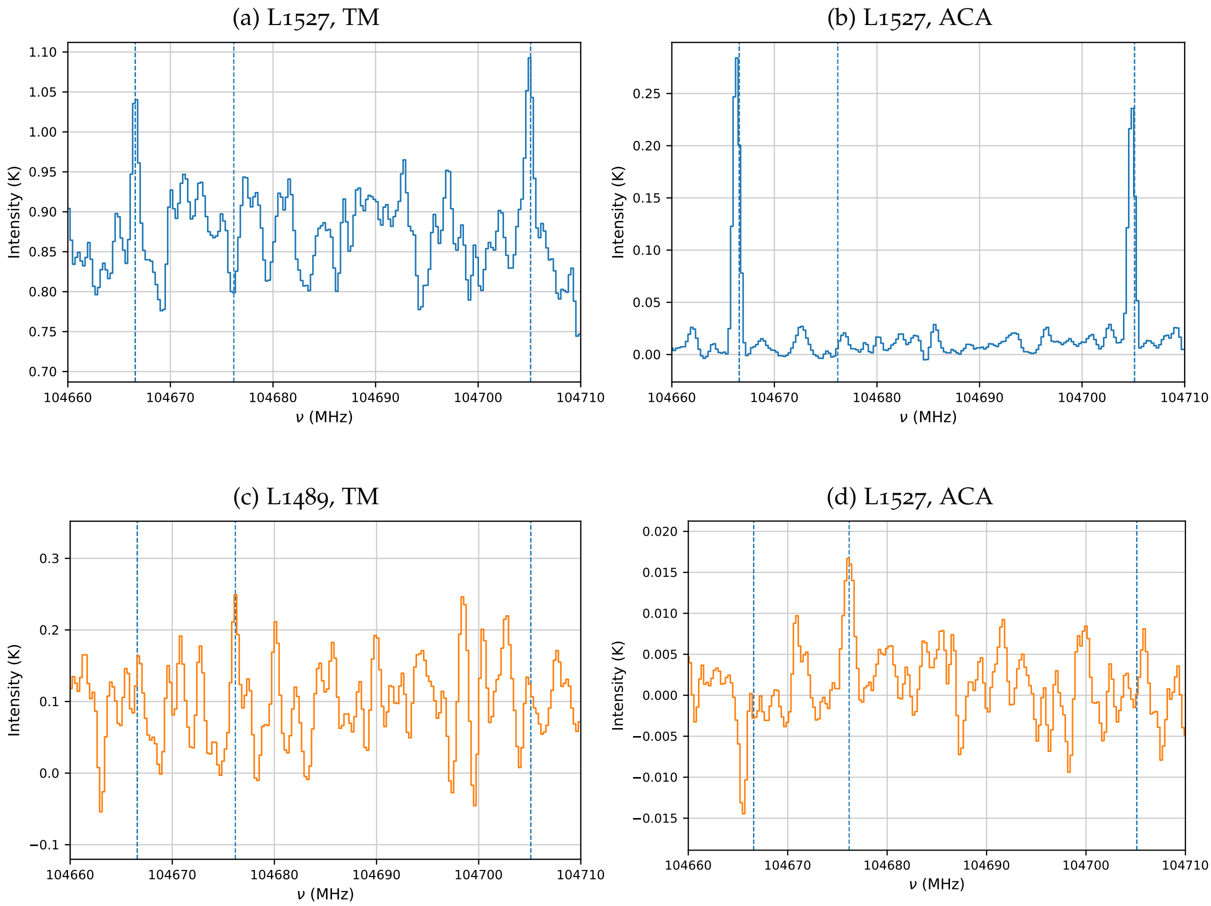

Figure 9: Detected lines for C_4H.

(a) L1527, ACA, C_4H.

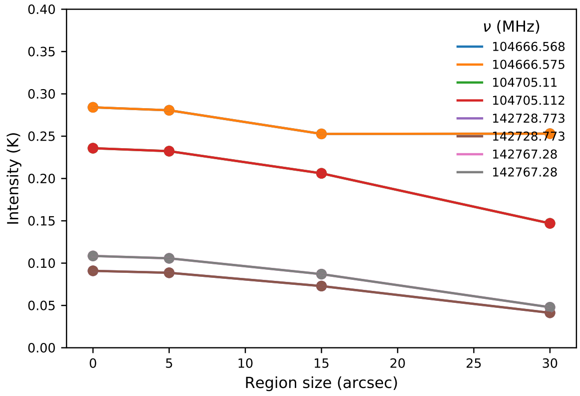

(b) L1527, TM, C_4H.

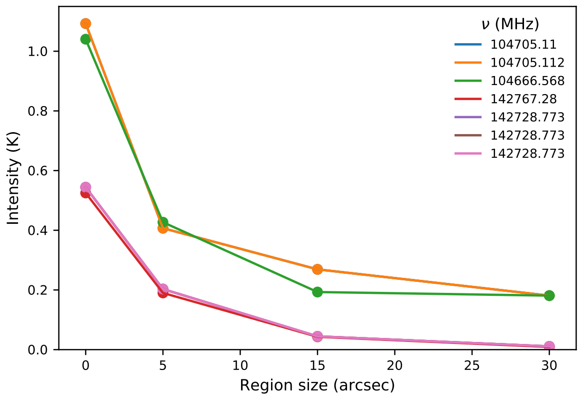

(c) L1489, ACA, C_4H.

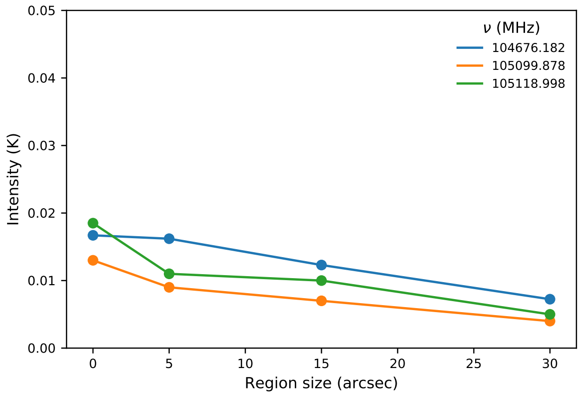

(d) L1489, TM, C_4H.

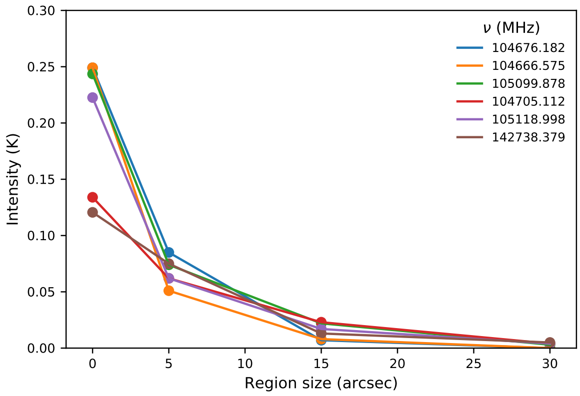

Figure 10: The way in which intensity decreases towards the outer edge of the regions, seems to be the same across all spectra. Therefore, only C_4H is displayed in this figure.

(a) L1527, ACA, C_4H.

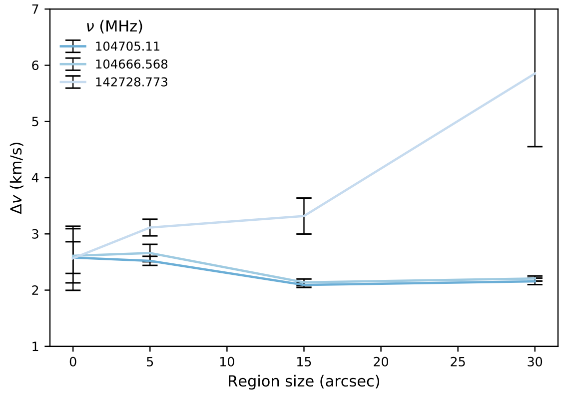

(b) L1527, TM, C_4H.

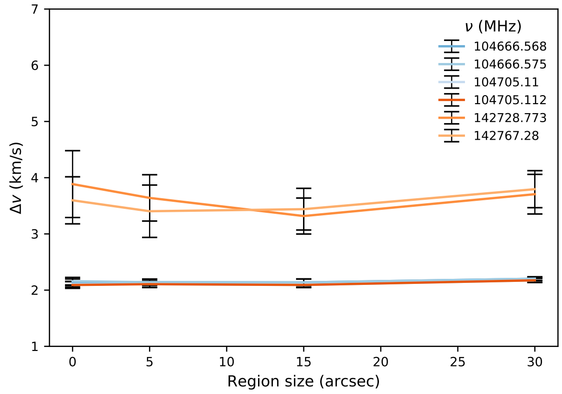

(c) L1489, ACA, C_4H.

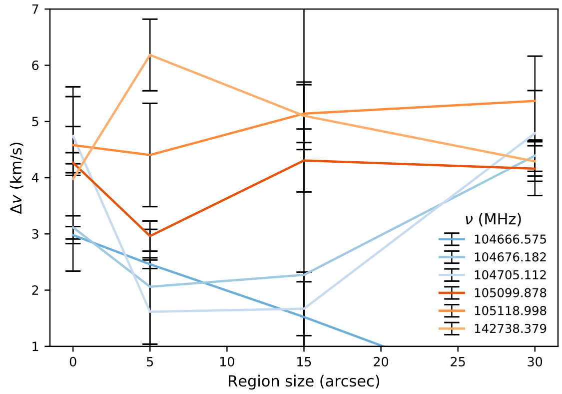

(d) L1489, TM, C_4H.

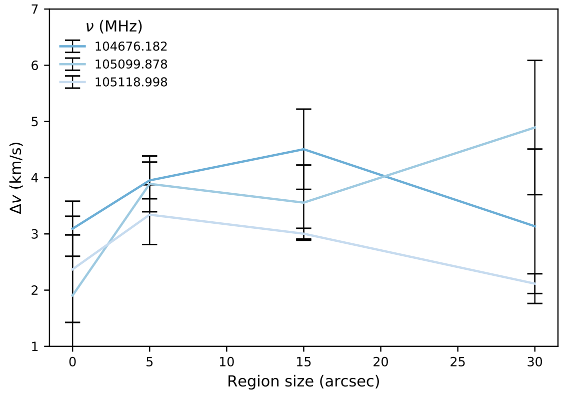

Figure 11: Detected lines for C_4H. Figures (a) and (b) seem to suggest a constant line width from the central to the outer regions of the disk for C_4H, with the exception of the $\nu = 142728.773$ MHz line. In figure (d) we can see a slight increase of line width from the center of the star towards a region of 15 arcsec around the center.

the N=15-14 transition. The measured velocities for the first two transitions do not correspond to the systemic velocity, which is 7.2 km/s.

One of the L1527 c-C_3H_2 transitions (N=12-11) has a ν_0 of 7.2, which is much higher than any of the other observed velocities (also for other species). This might be due to noise, but the line might also be caused by another species. n-C_3H_7CN would be a candidate (figure 12).

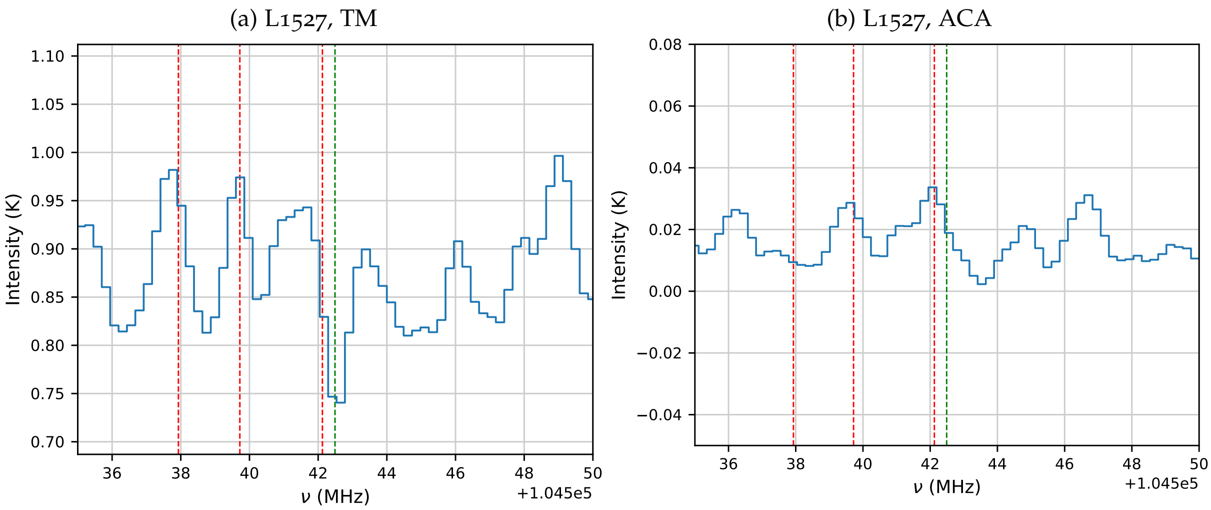

Figure 12: L1527, c-C_3H_2 (green) and n-C_3H_7CN lines (red). The lines of n-C_3H_7CN seem to correspond to other peaks as well.

l-C_3H_2

The two transitions of l-C_3H_2 are detected towards L1527 as well as L1489. In L1489 (TM), the N=5-4 transition has an observed velocity $\nu_0 = 6.2 \pm 0.2$ km/s, the second transition (N=7-6, L1489, TM) has $\nu_0 = 7.4 \pm 0.4$ km/s. For L1527, $\nu_0 = 6.3 \pm 0.04$ km/s (N=5-4) and $\nu_0 = 6.0 \pm 0.3$ km/s (N=7-6) in the ACA data, but $\nu_0 = 7.4 \pm 0.3$ km/s and $\nu_0 = 5.3 \pm 0.6$ km/s in the TM data. The second value is close to the velocity of the system. The value for the N=5-4 transition is in both cases higher than the systemic velocity. The peak intensity of the first transition is measured to be 1 K in L1527 and 161 mK in L1489 (TM data).

HC_3N & HC_5N

HC_3N was detected in L1527. The detection in L1489 is doubted, since another bright species (c-C_3HCN) has a transition close-by. In L1489, ACA, there are two peaks visible to the left and right of the position of this line. In the TM data, these lines seem to be blended together more, and might indicate the presence of another molecule than HC_3N contributing to this line.

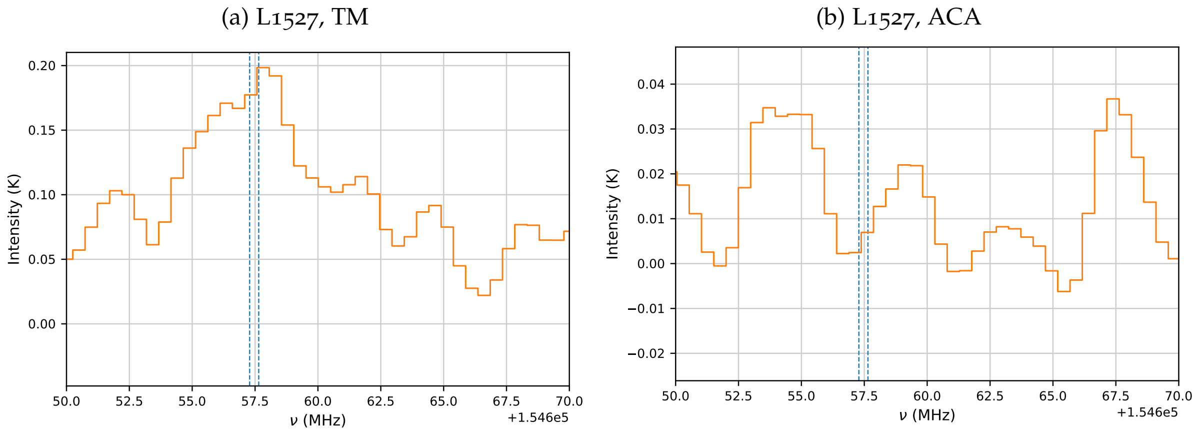

Figure 13: HC_3N and the nearby line of (c-C_3HCN). Figure 13b clearly shows a double peak around the expected position of the line.

Line broadening

The signal to noise level for the line width and region size relationships are too low to draw a conclusion about the broadening of the lines with region size. The brightest C_4H lines indicate that there is no noticeable difference between the line widths of L1527 and L1489, nor between ACA and TM data (see figure 11).

When we look at line width as a function of region size (distance from the central pixel, see figures 11, 15, and 14), we see that some of the molecules remain of constant line width. This is especially clear for C_4H and C_6H. The signal to noise ration for the detected lines of C_6H is low. Due to the low signal to noise ratio, the results at the outer edges of the field of view might be limited. For the inner region (until 5 arcsec), line width is mostly seen to increase or remain constant. With the exception of l-C_3H_2, HC_3N in the L1489 TM data, which decreases.

(a) L1527, $c-C_3H_2$. (b) L1489, $c-C_3H_2$.

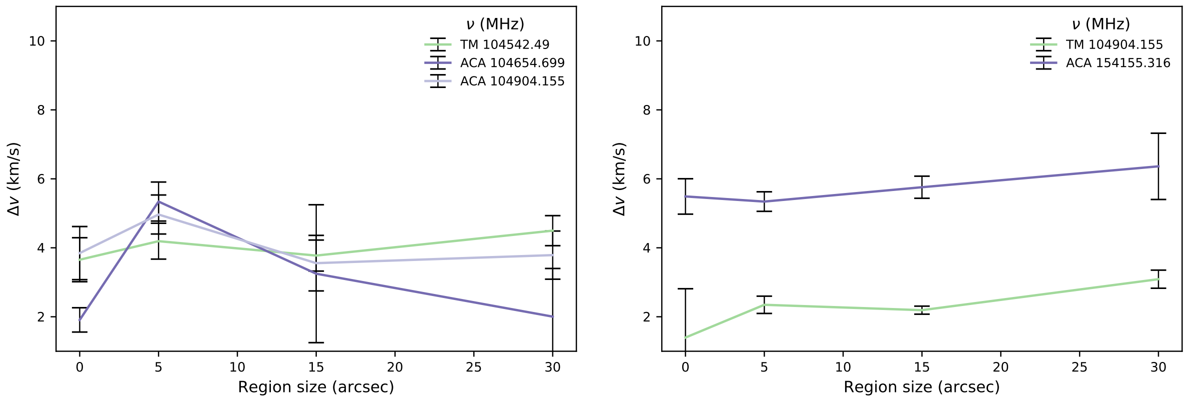

Figure 14: Linewidth as a function of distance from the center of the protostar. For L1527, the linewidth seems to increase at first and remain constant beyond 15 arcsec. For L1489, the linewidth is constant.

(a) L1527, HC_3N. (b) L1489, HC_3N.

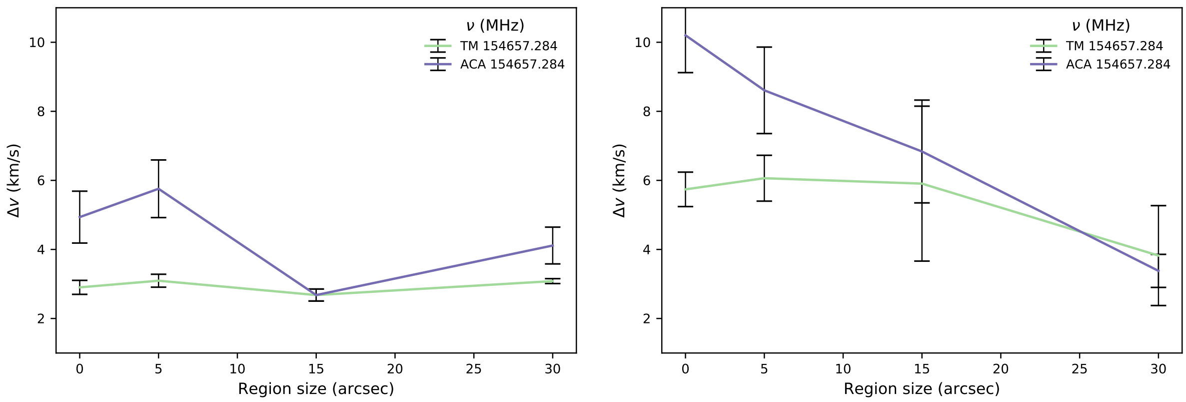

Figure 15: From the L1527 data, it would seem that HC_3N has a constant linewidth over all regions. Before 5 arcsec, the value remains constant, after which it decreases towards 30 arcsec. For L1489 (b), the linewidth decreases over region size.

(a) L1527, ACA, $c-C_3HD$.

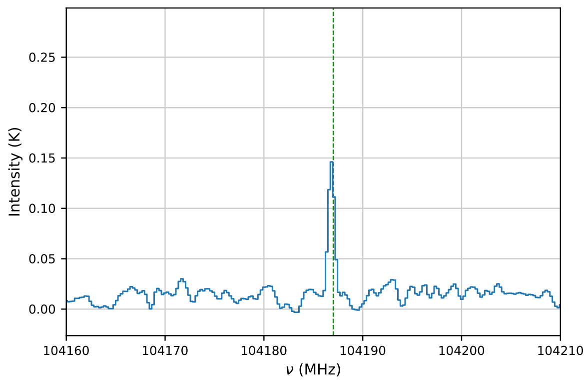

(b) L1527, TM, $c-C_3HD$.

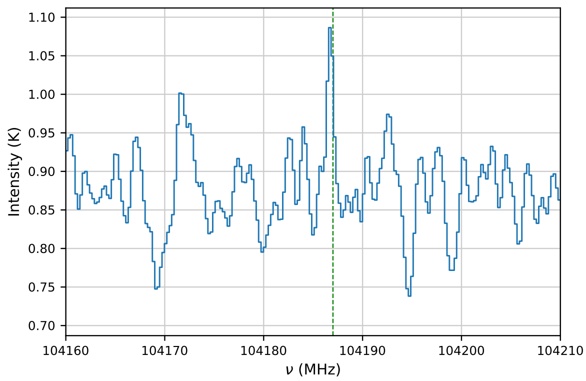

(c) L1489, ACA, $c-C_3HD$.

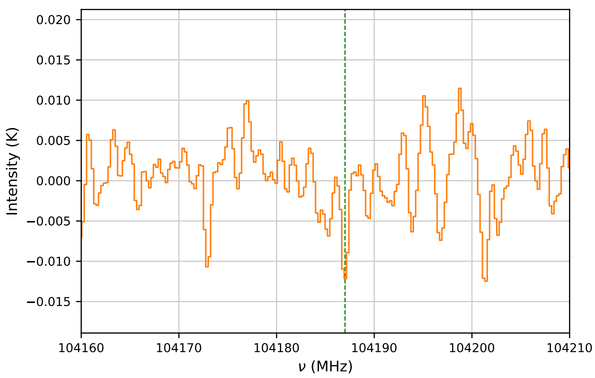

(d) L1489, TM, $c-C_3HD$.

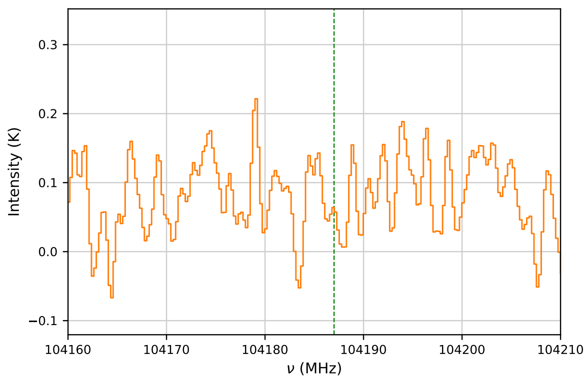

Figure 16: The spectra around $c-C_3HD$ at $\nu_0 = 104.187$ GHz.

Table 4: Comparison of all detected transitions.

Species	Transition	ν_0 (MHz)	L1489 ACA	L1489 TM	L1527 ACA	L1527 TM
C_4H	(11 11.5 11 _ 10 10.5 10)	104666.568		✓	✓	✓
C_4H	(11 11.5 12 _ 10 10.5 11)	104666.575		✓	✓	✓
C_4H	(11 11.5 11 _ 10 10.5 11)	104676.178	✓	✓		
C_4H	(11 10.5 10 _ 10 9.5 9)	104705.11			✓	✓
C_4H	(11 10.5 11 _ 10 9.5 10)	104705.112		~	✓	✓
C_4H	(11 10.5 10 _ 10 10.5 10)	105099.874	✓	✓		
C_4H	(11 10.5 11 _ 10 10.5 11)	105118.993	✓	~		
C_4H	(15 15.5 15 _ 14 14.5 14)	142728.773			✓	✓
C_4H	(15 15.5 16 _ 14 14.5 15)	142728.773			✓	✓
C_4H	(15 15.5 15 _ 14 14.5 15)	142738.379		~		
C_4H	(15 14.5 14 _ 14 13.5 13)	142767.28			✓	
C_4H	(15 14.5 15 _ 14 13.5 14)	142767.28			✓	
$l-C_3H_2$	(5 1 4 _ 4 1 3)	104915.583	~	✓	✓	✓
$l-C_3H_2$	(7 1 7 _ 6 1 6)	144183.804		✓	✓	✓
$c-C_3H_2$	(8 8 1 0 _ 8 7 2 0)	104904.155	✓			✓
$c-C_3H_2$	(3 3 0 0 _ 3 0 3 0)	154155.316		✓		
$c-C_3H_2$	(15 6 10 0 _ 14 7 7 0)	154599.424		~		
$c-C_3H_2$	(16 12 4 0 _ 16 11 5 0)	104990.844			~	
$c-C_3H_2$	(12 6 7 0 _ 11 9 2 0)	104542.49			~	
$c-C_3H_2$	(11 10 1 0 _ 11 9 2 0)	104654.699				✓
C_6H	(52 2 -1 52 _ 51 2 1 51)	142820.509		~		?
C_6H	(52 2 -1 51 _ 51 2 1 51)	142820.829		~		?
C_6H	(56 2 1 55 _ 55 2 -1 54)	153841.385		?		✓
C_6H	(56 2 1 55 _ 55 2 -1 55)	153841.747		?		✓
C_6H	(55 1 55.5 _ 54 -1 54.5)	153841.342		?		✓
HC_3N	(17 _ 16)	154657.284	✓	✓	✓	✓

Table 5: L1527, ACA

Detected transitions for L1527, ACA

Species	Transition	Frequency (MHz)	E_{up} (K)	G_{up}	$A_{ij}(s^{-1})$	v_o (km/s)	Peak intensity (K)	Δv (km/s)
C_4H	(11 10.5 10 _ 10 9.5 9)	104705.11	30.1562	21	5.13E − 06	6.32 ± 0.02	0.24	2.1 ± 0.05
C_4H	(11 10.5 11 _ 10 9.5 10)	104705.112	30.1568	23	5.15E − 06	6.33 ± 0.02	0.24	2.09 ± 0.06
C_4H	(11 10.5 10 _ 10 10.5 10)	105099.874	30.1563	21	2.33E − 08		< 0.032	
C_4H	(11 10.5 11 _ 10 10.5 11)	105118.993	30.1568	23	2.20E − 08		< 0.032	
C_4H	(11 11.5 11 _ 10 10.5 10)	104666.568	30.1355	23	5.15E − 06	6.33 ± 0.02	0.28	2.14 ± 0.06
C_4H	(11 11.5 11 _ 10 10.5 11)	104676.178	30.1355	23	2.11E − 08		< 0.035	
C_4H	(11 11.5 12 _ 10 10.5 11)	104666.575	30.135	25	5.17E − 06	6.31 ± 0.03	0.28	2.16 ± 0.07
C_4H	(15 14.5 14 _ 14 13.5 13)	142767.28	54.8233	29	1.32E − 05	5.6 ± 0.17	0.11	3.6 ± 0.4
C_4H	(15 14.5 15 _ 14 13.5 14)	142767.28	54.8238	31	1.32E − 05	5.4 ± 0.14	0.11	4.4 ± 0.4
C_4H	(15 15.5 15 _ 14 14.5 14)	142728.773	54.7951	31	1.32E − 05	5.9 ± 0.23	0.09	3.9 ± 0.6
C_4H	(15 15.5 16 _ 14 14.5 15)	142728.773	54.7946	33	1.33E − 05	6.0 ± 0.25	0.09	3.9 ± 0.6
$c-C_3H_2$	(3 3 0 0 _ 3 0 3 0)	154155.316	19.466	21	4.09E − 07		< 0.074	
$c-C_3H_2$	(8 8 1 0 _ 8 7 2 0)	104904.155	118.5149	51	2.23E − 05		< 0.035	
$c-C_3H_2$	(11 10 1 0 _ 11 9 2 0)	104654.699	211.6387	69	3.51E − 05		< 0.035	
$c-C_3H_2$	(12 6 7 0 _ 11 9 2 0)	104542.49	211.6333	75	2.02E − 09	7.2 ± 0.18	0.03	3.7 ± 0.6
$c-C_3H_2$	(15 6 10 0 _ 14 7 7 0)	154599.424	305.7983	31	8.47E − 08		< 0.074	
$c-C_3H_2$	(16 12 4 0 _ 16 11 5 0)	104990.844	420.3821	33	5.93E − 05	5.9 ± 0.24	0.03	
$l-C_3H_2$	(5 1 4 _ 4 1 3)	104915.583	28.4646	33	9.86E − 05	6.3 ± 0.04	0.06	1.9 ± 0.1
$l-C_3H_2$	(7 1 7 _ 6 1 6)	144183.804	41.0388	45	2.68E − 04	6.0 ± 0.26	0.09	4.5 ± 0.3
C_6H	(56 2 1 55 _ 55 2 -1 54)	153841.385	208.3383	111	7.30E − 04		< 0.074	
C_6H	(56 2 1 55 _ 55 2 -1 55)	153841.747	208.3383	111	1.20E − 07		< 0.074	
C_6H	(55 1 55.5 _ 54 -1 54.5)	153841.342					< 0.074	
HC_3N	(17 _ 16)	154657.284	66.8036	35	2.91E − 04	6.3 ± 0.08	0.21	2.9 ± 0.2

Detected transitions for L1527, TM

Species	Transition	Frequency (MHz)	E_{up} (K)	G_{up}	$A_{ij}(s^{-1})$	ν_o (km/s)	Peak intensity (K)	$\Delta\nu$ (km/s)
C_4H	(11 10.5 10 _ 10 9.5 9)	104705.11	30.1562	21	5.13E − 06	5.9 ± 0.2	1.09	2.6 ± 0.3
C_4H	(11 10.5 11 _ 10 9.5 10)	104705.112	30.1568	23	5.15E − 06	5.9 ± 0.2	1.09	2.6 ± 0.3
C_4H	(11 10.5 10 _ 10 10.5 10)	105099.874	30.1563	21	2.33E − 08		< 1.02	
C_4H	(11 10.5 11 _ 10 10.5 11)	105118.993	30.1568	23	2.20E − 08		< 1.02	
C_4H	(11 11.5 11 _ 10 10.5 10)	104666.568	30.1355	23	5.15E − 06	5.4 ± 0.2	1.04	2.6 ± 0.5
C_4H	(11 11.5 11 _ 10 10.5 11)	104676.178	30.1355	23	2.11E − 08		< 0.99	
C_4H	(11 11.5 12 _ 10 10.5 11)	104666.575	30.135	25	5.17E − 06	5.4 ± 0.2	1.04	2.6 ± 0.5
C_4H	(15 14.5 14 _ 14 13.5 13)	142767.28	54.8233	29	1.32E − 05		< 0.55	
C_4H	(15 14.5 15 _ 14 13.5 14)	142767.28	54.8238	31	1.32E − 05		< 0.55	
C_4H	(15 15.5 15 _ 14 14.5 14)	142728.773	54.7951	31	1.32E − 05	5.4 ± 0.4	0.54	2.6 ± 0.6
C_4H	(15 15.5 16 _ 14 14.5 15)	142728.773	54.7946	33	1.33E − 05	5.4 ± 0.4	0.54	2.6 ± 0.6
$c-C_3H_2$	(3 3 0 0 _ 3 0 3 0)	154155.316	19.466	21	4.09E − 07		< 0.64	
$c-C_3H_2$	(8 8 1 0 _ 8 7 2 0)	104904.155	118.5149	51	2.23E − 05	7.1 ± 0.3	0.93	3.9 ± 0.8
$c-C_3H_2$	(11 10 1 0 _ 11 9 2 0)	104654.699	211.6387	69	3.51E − 05	6.0 ± 0.1	0.88	1.9 ± 0.4
$c-C_3H_2$	(12 6 7 0 _ 11 9 2 0)	104542.49	211.6333	75	2.02E − 09		< 0.99	
$c-C_3H_2$	(15 6 10 0 _ 14 7 7 0)	154599.424	305.7983	31	8.47E − 08		< 0.64	
$c-C_3H_2$	(16 12 4 0 _ 16 11 5 0)	104990.844	420.3821	33	5.93E − 05		< 1.02	
$l-C_3H_2$	(5 1 4 _ 4 1 3)	104915.583	28.4646	33	9.86E − 05	7.4 ± 0.3	1.00	3.2 ± 1.1
$l-C_3H_2$	(7 1 7 _ 6 1 6)	144183.804	41.0388	45	2.68E − 04	5.3 ± 0.6	0.54	4.2 ± 0.2
C_6H	(56 2 1 55 _ 55 2 -1 54)	153841.385	208.3383	111	7.30E − 04	5.7 ± 0.5	0.64	4.0 ± 1.0
C_6H	(56 2 1 55 _ 55 2 -1 55)	153841.747	208.3383	111	1.20E − 07	5.4 ± 0.1	0.64	3.7 ± 0.3
C_6H	(55 1 55.5 _ 54 -1 54.5)	153841.342					< 0.64	
HC_3N	(17 _ 16)	154657.284	66.8036	35	2.91E − 04	6.0 ± 0.3	0.73	4.9 ± 0.8

Table 6: L1527, TM

Table 7: L1489, ACA

Detected transitions for L1489, ACA								
Species	Transition	Frequency (MHz)	E_{up} (K)	G_{up}	$A_{ij}(s^{-1})$	ν_o (km/s)	Peak intensity (K)	$\Delta\nu$ (km/s)
C_4H	(11 10.5 10 _ 10 9.5 9)	104705.11	30.1562	21	$5.13E-06$		< 0.013	
C_4H	(11 10.5 11 _ 10 9.5 10)	104705.112	30.1568	23	$5.15E-06$		< 0.013	
C_4H	(11 10.5 10 _ 10 10.5 10)	105099.874	30.1563	21	$2.33E-08$	8.5 ± 0.5	0.013	1.9 ± 1.1
C_4H	(11 10.5 11 _ 10 10.5 11)	105118.993	30.1568	23	$2.20E-08$	4.3 ± 0.4	0.019	2.4 ± 0.9
C_4H	(11 11.5 11 _ 10 10.5 10)	104666.568	30.1355	23	$5.15E-06$		< 0.013	
C_4H	(11 11.5 11 _ 10 10.5 11)	104676.178	30.1355	23	$2.11E-08$	7.0 ± 0.2	0.017	3.1 ± 0.5
C_4H	(11 11.5 12 _ 10 10.5 11)	104666.575	30.135	25	$5.17E-06$		< 0.013	
C_4H	(15 14.5 14 _ 14 13.5 13)	142767.28	54.8233	29	$1.32E-05$		< 0.036	
C_4H	(15 14.5 15 _ 14 13.5 14)	142767.28	54.8238	31	$1.32E-05$		< 0.036	
C_4H	(15 15.5 15 _ 14 14.5 14)	142728.773	54.7951	31	$1.32E-05$		< 0.036	
C_4H	(15 15.5 16 _ 14 14.5 15)	142728.773	54.7946	33	$1.33E-05$		< 0.036	
$c-C_3H_2$	(3 3 0 0 _ 3 0 3 0)	154155.316	19.466	21	$4.09E-07$		< 0.031	
$c-C_3H_2$	(8 8 1 0 _ 8 7 2 0)	104904.155	118.5149	51	$2.23E-05$	8.7 ± 0.6	0.014	1.4 ± 1.4
$c-C_3H_2$	(11 10 1 0 _ 11 9 2 0)	104654.699	211.6387	69	$3.51E-05$		< 0.013	
$c-C_3H_2$	(12 6 7 0 _ 11 9 2 0)	104542.49	211.6333	75	$2.02E-09$		< 0.013	
$c-C_3H_2$	(15 6 10 0 _ 14 7 7 0)	154599.424	305.7983	31	$8.47E-08$		< 0.031	
$c-C_3H_2$	(16 12 4 0 _ 16 11 5 0)	104990.844	420.3821	33	$5.93E-05$		< 0.013	
$l-C_3H_2$	(5 1 4 _ 4 1 3)	104915.583	28.4646	33	$9.86E-05$		< 0.013	
$l-C_3H_2$	(7 1 7 _ 6 1 6)	144183.804	41.0388	45	$2.68E-04$		< 0.036	
C_6H	(56 2 1 55 _ 55 2 -1 54)	153841.385	208.3383	111	$7.30E-04$		< 0.031	
C_6H	(56 2 1 55 _ 55 2 -1 55)	153841.747	208.3383	111	$1.20E-07$		< 0.031	
C_6H	(55 1 55.5 _ 54 -1 54.5)	153841.342					< 0.031	
HC_3N	(17 _ 16)	154657.284	66.8036	35	$2.91E-04$	11.4 ± 0.2	0.035	5.7 ± 0.5

Detected transitions for L1489, TM

Species	Transition	Frequency (MHz)	E_{up} (K)	G_{up}	$A_{ij}(s^{-1})$	ν_o (km/s)	Peak intensity (K)	$\Delta\nu$ (km/s)
C_4H	(11 10.5 10 _ 10 9.5 9)	104705.11	30.1562	21	5.13E − 06		< 0.26	
C_4H	(11 10.5 11 _ 10 9.5 10)	104705.112	30.1568	23	5.15E − 06		< 0.26	
C_4H	(11 10.5 10 _ 10 10.5 10)	105099.874	30.1563	21	2.33E − 08	9.3 ± 0.5	0.244	4.3 ± 0.2
C_4H	(11 10.5 11 _ 10 10.5 11)	105118.993	30.1568	23	2.20E − 08	10.1 ± 0.4	0.223	4.6 ± 0.3
C_4H	(11 11.5 11 _ 10 10.5 10)	104666.568	30.1355	23	5.15E − 06		< 0.26	
C_4H	(11 11.5 11 _ 10 10.5 11)	104676.178	30.1355	23	2.11E − 08	6.9 ± 0.3	0.249	3.1 ± 0.2
C_4H	(11 11.5 12 _ 10 10.5 11)	104666.575	30.135	25	5.17E − 06	6.3 ± 0.5	0.249	3.0 ± 0.2
C_4H	(15 14.5 14 _ 14 13.5 13)	142767.28	54.8233	29	1.32E − 05		< 0.13	
C_4H	(15 14.5 15 _ 14 13.5 14)	142767.28	54.8238	31	1.32E − 05		< 0.13	
C_4H	(15 15.5 15 _ 14 14.5 14)	142728.773	54.7951	31	1.32E − 05		< 0.13	
C_4H	(15 15.5 16 _ 14 14.5 15)	142728.773	54.7946	33	1.33E − 05	6.4 ± 0.5	0.121	4.0 ± 1.6
$c-C_3H_2$	(3 3 0 0 _ 3 0 3 0)	154155.316	19.466	21	4.09E − 07	4.6 ± 0.5	0.152	8.0 ± 0.2
$c-C_3H_2$	(8 8 1 0 _ 8 7 2 0)	104904.155	118.5149	51	2.23E − 05		< 0.26	
$c-C_3H_2$	(11 10 1 0 _ 11 9 2 0)	104654.699	211.6387	69	3.51E − 05		< 0.26	
$c-C_3H_2$	(12 6 7 0 _ 11 9 2 0)	104542.49	211.6333	75	2.02E − 09		< 0.26	
$c-C_3H_2$	(15 6 10 0 _ 14 7 7 0)	154599.424	305.7983	31	8.47E − 08	7.2 ± 0.9	0.142	6.6 ± 0.2
$c-C_3H_2$	(16 12 4 0 _ 16 11 5 0)	104990.844	420.3821	33	5.93E − 05		< 0.26	
$l-C_3H_2$	(5 1 4 _ 4 1 3)	104915.583	28.4646	33	9.86E − 05	6.2 ± 0.2	0.161	2.8 ± 0.9
$l-C_3H_2$	(7 1 7 _ 6 1 6)	144183.804	41.0388	45	2.68E − 04	7.4 ± 0.4	0.101	5.0 ± 1.3
C_6H	(56 2 1 55 _ 55 2 -1 54)	153841.385	208.3383	111	7.30E − 04		< 0.15	
C_6H	(56 2 1 55 _ 55 2 -1 55)	153841.747	208.3383	111	1.20E − 07		< 0.15	
C_6H	(55 1 55.5 _ 54 -1 54.5)	153841.342					< 0.15	
HC_3N	(17 _ 16)	154657.284	66.8036	35	2.91E − 04	6.4 ± 0.4	0.198	10.2 ± 1.1

Table 8: L1489, TM

5 DISCUSSION AND CONCLUSION

In this chapter we discuss the results and conclude what the detected species tell us about the observed protostellar systems. First we take a look at the detected transitions, and compare the two protostellar systems and the ALMA arrays. Then, we discuss what the detected line strengths and widths mean for the structure and the chemistry of the protoplanetary disks. Finally, we discuss remaining questions and possibilities for future work.

5.1 DETECTED TRANSITIONS

L1527 shows clear C_4H transitions in the data. The lines in band 3, spectral window 3 (TM), have the same velocity ($\nu_0 \approx 6.3$ km/s). The lines in band 4 show lower velocities from $\nu_0 \approx 5.4$ km/s to $\nu_0 \approx 6.0$ km/s. For L1489, only one transition of C_4H was detected with more than 3σ confidence (ACA: > 0.013 K, TM: > 0.26 K) (11 11.5 11 - 10 10.5 11) at 104676.178 MHz). This transition was detected in both TM as well as in ACA data. The TM data shows lines at two other frequencies as well. The difference between L1527 and L1489 for C_4H is that in L1489 we only detect a couple of high-excitation lines instead of ones with lower energy levels. This seems to be the case for c-C_3H_2 and l-C_3H_2 as well. L1527 also shows the lower transitions. For this reason, we expect that L1489 has a more massive protostar than L1527, resulting in higher temperatures for molecules that are formed close to the center. The star in L1527 is of a lower mass and chemical reactions take place at relatively moderate temperatures.

5.2 VELOCITY SHIFTS

Shifts in the velocities of molecular line profiles might be caused by motions of a turbulent nature within the molecular cloud. These motions are most likely a combination of collapse, rotation, or random motions ([15]). This causes variations in the characteristic velocities of detected transitions. We expect these velocity shifts to stay within the order of 0.5 kms^{-1}, based on previous results by Sakai et al. [19].

However, not all velocity shifts indicate motions within the object. We summarized these lines in table 9. These are likely to be false detection since their velocity offset is much higher or lower than the expected value.

All C_4H lines in L1527 in band 3 have a ν_0 of 6.3 km/s. The lines in band 4 show a value closer to the ν_{LSR} of the source (5.8 km/s). The

Table 9: The detected lines with high-offset characteristic velocities for L1489 and L1527.

L1527 ($v_0 = 5.85$ km/s)			
Array	Species	Transition	v_0 (km/s)
ACA	c-C_3H_2	(12 6 7 _11 9 2)	7.2 ± 0.2
TM	c-C_3H_2	(8 8 1 _ 8 7 2)	7.1 ± 0.3
TM	l-C_3H_2	(5 1 4 _ 4 1 3)	7.4 ± 0.3
L1489 ($v_0 = 7.2$ km/s)			
Array	Species	Transition	v_0 (km/s)
ACA	C_4H	(11 10.5 10 _ 10 10.5 10)	8.5 ± 0.5
ACA	C_4H	(11 10.5 11 _ 10 10.5 11)	4.3 ± 0.4
ACA	c-C_3H_2	(8 8 1 0 _ 8 7 2 0)	8.7 ± 0.6
ACA	HC_3N	(17 _ 16)	11.4 ± 0.2
TM	C_4H	(11 10.5 10 _ 10 10.5 10)	9.3 ± 0.5
TM	C_4H	(11 10.5 11 _ 10 10.5 11)	10.1 ± 0.4
TM	c-C_3H_2	(3 3 0 0 _ 3 0 3 0)	4.6 ± 0.5
TM	l-C_3H_2	(5 1 4 _ 4 1 3)	6.2 ± 0.2

band 3 transitions of C_4H indicate an that they (also) exist in more outlying regions, while the band 4 transitions (with higher E_{up}) are only present closer to the protostar. Sakai et al. [19] mention that the velocities in L1527 are not significantly different from the systemic velocity. This would indicate that the radiation is emitted from the inner part of the core, not from the surrounding gas.

5.3 COMPARISON TO PREVIOUS RESEARCH

High-excitation lines of C_4H have previously been observed towards L1527, as well as l-C_3H_2 and c-C_3H_2 [19]. Sakai et al. [19] also found (weaker) lines for C_5H and HC_5N. The line intensities that they found for C_4H are 1.6-1.7 K. They mention that C_4H has an increase in line width toward the center. They were also the first to detect longer carbon-chain molecules such as C_5H and HC_7N. This corresponds to our findings. Various carbon-chain molecules have been detected towards L1527. C_4H and C_4H_2 have bright lines. Other observed CC-molecules in L1527 are C_6H, C_6H_2, HC_7N, and HC_9N [18]. There are not many previous detections of CC molecules in L1489.

5.4 COMPARISON BETWEEN SOURCES

The C_4H lines in L1527 are about 4 times stronger in intensity than in L1489. L1489 is the brightest source of the two (in bolometric luminosity). So the apparent brightness of the object does not play a role in the lack of some of the lines in L1489.

However, it is notable that the observed C_4H transitions in L1489 are of a different intensity ratio than the ones in L1527. Particularly, the notable double C_4H pattern in L1527 is not visible in L1489, even though these two peaks have the lowest upper energy level and are expected to show high peaks. The strongest C_4H peak in L1489 does not occur in the spectrum of L1527. Perhaps this means that the line observed in L1489 is (partially) caused by another species. However, we were unable to find candidates in the molecular databases (JPL and CDMS) around $\nu = 104676$ MHz.

Long carbon-chain molecules (C_6H, HC_5N) were difficult to find. C_6H potentially has some peaks in L1527 but HC_5N was not found. Detecting them would be surprising, because most of the transitions would be too weak to be visible above the noise level.

Even though c-C_3HD was not on our CC-molecule list, we found it to be present in L1527 with a bright peak of 0.15K (ACA, central pixel) or 1.10K (TM, central pixel). c-C_3HD is not present in L1489.

The lack of some of the c-C_3H_2 transitions among both sources can be caused by the high level of noise. Some of the lines that were not counted as a detection, small peaks were visible slightly below the 3σ threshold.

The fact that L1489 contains less carbon-chain molecules, could mean that the object is in a later stage of evolution than L1527. L1527 is very young, there is a lot of material in the envelope, the core is less obscured. A lot of mass is still moving around in the envelope and forming new molecules. L1489 is already further along the evolutionary track, meaning that the protostar is more massive and the envelope less dense. There is less carbon-chain chemistry going on in the protostellar neighbourhood. It would also mean the temperature is higher and thus that L1489 is more luminous. Sakai et al. ([19]) suggest that carbon-chain molecules could survive when the freefall collapse happens fast enough, not allowing chemical reactions to take place. Since CC-molecules of the C_nC_m form seem to be more abundant than others, they might have a longer lifetime ([19]). The fact that the further along its evolutionary track the protostar is, the less CC-molecules we detect is understandable if we suppose that most CC molecules are found in cold, dark regions such as starless cores [24]. When there is more stellar radiation and an increase in temperature, the availability of molecules necessary for carbon-chain chemistry will decrease, as well as the conditions for reactions to take place.

The abundance of HC_nN can be dedicated to a usually slower formation process (Turner et al. 1998, [19]).

5.5 COMPARISON BETWEEN ACA AND TM DATA

The ACA data generally contains less lines that the TM data. Especially L1489 has almost no detections in the ACA data. This means that the CC-molecules have a lower intensity (relative to other emission) in the large-scale emission of the source. The lower excitation lines are usually more extended [19] and their peak temperature is therefore lower.

5.6 CONCLUSION

In the end, we can conclude that carbon-chain molecules are present in the protoplanetary systems L1527 and L1489. Especially C_4H is a recognizable feature extended over the entire radius of the protostar and disk.

In summary, we have found that:

1. C_4H, C_6H, l-C_3H_2, c-C_3H_2, and HC_3N are detected toward L1527
2. C_4H, l-C_3H_2, and c-C_3H_2 are detected toward L1489
3. L1527 contains a wider variety of CC molecules than L1489
4. The intensity of CC molecules increases toward the center of the protostellar system
5. There is no notable difference in line width between L1527 and L1489
6. L1489 has more high-excitation peaks than lower ones
7. L1489 is older and the protostar is more massive than L1527, L1489 is further along its evolutionary track and has already absorbed more of the envelope material than L1527.

BIBLIOGRAPHY

[1] P. Andre, D. Ward-Thompson, and M. Barsony. "From Prestellar Cores to Protostars: the Initial Conditions of Star Formation." In: *Protostars and Planets IV* (May 2000), p. 59. eprint: astro-ph/9903284.

[2] Brinch, C., Crapsi, A., Hogerheijde, M. R., and Jorgensen, J. K. "Structure and dynamics of the class I young stellar object L1489 IRS." In: *Astronomy and Astrophysics* 461.3 (2007), pp. 1037–1047. DOI: 10.1051/0004-6361:20065473. URL: https://doi.org/10.1051/0004-6361:20065473.

[3] Ewine F van Dishoeck. "Chemistry in low-mass protostellar and protoplanetary regions." In: *Proceedings of the National Academy of Sciences of the United States of America* 103.33 (2006), pp. 12249–56. ISSN: 0027-8424. DOI: 10.1073/pnas.0602207103. URL: http://www.pnas.org/content/103/33/12249.abstract.

[4] Ewine F. van Dishoeck. "Astrochemistry of Dense Protostellar and Protoplanetary Environments." In: (2009), pp. 187–213. DOI: 10.1007/978-1-4020-9457-6_8.

[5] Ewine F. van Dishoeck and Geoffrey A. Blake. "CHEMICAL EVOLUTION OF STAR-FORMING REGIONS." In: *Annual Review of Astronomy and Astrophysics* 36.1 (1998), pp. 317–368. DOI: 10.1146/annurev.astro.36.1.317. eprint: https://doi.org/10.1146/annurev.astro.36.1.317. URL: https://doi.org/10.1146/annurev.astro.36.1.317.

[6] Neal J. Evans. "Physical Conditions in Regions of Star Formation." In: 37 (1999), pp. 311–62. ISSN: 0066-4146. DOI: 10.1146/annurev.astro.37.1.311. eprint: 9905050.

[7] Adam Ginsburg, Brett McGuire, Richard Plambeck, John Bally, Ciriaco Goddi, and Melvyn Wright. "Orion SrcI's Disk Is Salty." In: *The Astrophysical Journal* 872.1 (Feb. 2019), p. 54. DOI: 10.3847/1538-4357/aafb71. URL: https://doi.org/10.3847%2F1538-4357%2Faafb71.

[8] Eric Herbst and Ewine F. van Dishoeck. "Complex Organic Interstellar Molecules." In: *Annual Review of Astronomy and Astrophysics* 47.1 (2009), pp. 427–480. DOI: 10.1146/annurev-astro-082708-101654. eprint: https://doi.org/10.1146/annurev-astro-082708-101654. URL: https://doi.org/10.1146/annurev-astro-082708-101654.

[9] Michiel R. Hogerheijde. "From Infall to Rotation around Young Stellar Objects: A Transitional Phase with a 2000 AU Radius Contracting Disk?" In: *The Astrophysical Journal* 553.2 (June 2001), pp. 618–632. DOI: 10.1086/320972. arXiv: astro-ph/0101569 [astro-ph].

[10] Michiel R. Hogerheijde, Ewine F. van Dishoeck, Geoffrey A. Blake, and Huib Jan van Langevelde. "Envelope Structure on 700 AU Scales and the Molecular Outflows of Low-Mass Young Stellar Objects." In: *The Astrophysical Journal* 502.1 (1998), pp. 315–336. DOI: 10.1086/305885. URL: https://doi.org/10.1086%2F305885.

[11] Jørgensen, J. K. et al. "The ALMA Protostellar Interferometric Line Survey (PILS) - First results from an unbiased submillimeter wavelength line survey of the Class 0 protostellar binary IRAS 16293-2422 with ALMA." In: *A&A* 595 (2016), A117. DOI: 10.1051/0004-6361/201628648. URL: https://doi.org/10.1051/0004-6361/201628648.

[12] Jes K. Jorgensen, Ewine F. van Dishoeck, Ruud Visser, Tyler L. Bourke, David J. Wilner, Dave Lommen, Michiel R. Hogerheijde, and Philip C. Myers. "PROSAC: A Submillimeter Array survey of low-mass protostars. II. The mass evolution of envelopes, disks, and stars from the Class 0 through I stages." In: 879 (2009), pp. 861–879. DOI: 10.1051/0004-6361/200912325. eprint: 0909.3386. URL: http://arxiv.org/abs/0909.3386{\%}0Ahttp://dx.doi.org/10.1051/0004-6361/200912325.

[13] Robert C. Kennicutt and Neal J. Evans. "Star Formation in the Milky Way and Nearby Galaxies." In: *Annual Review of Astronomy and Astrophysics* 50 (Sept. 2012), pp. 531–608. DOI: 10.1146/annurev-astro-081811-125610. arXiv: 1204.3552 [astro-ph.GA].

[14] Charles J Lada and N D Kylafis. "The Origin of Stars and Planetary Systems." In: *Proceedings of the NATO Advanced Study Institute, The Physics of Star Formation and Early Evolution-II, held in Crete, Greece, 24 May-5 June, 1998*. 1999, p. 202. ISBN: 9789401145091. DOI: 978-94-011-4509-1.

[15] R. B. Larson. "Turbulence and star formation in molecular clouds." In: *MNRAS* 194 (Mar. 1981), pp. 809–826. DOI: 10.1093/mnras/194.4.809.

[16] Charles J. Law, Karin I. Öberg, Jennifer B. Bergner, and Dawn Graninger. "Carbon Chain Molecules toward Embedded Low-mass Protostars." In: *The Astrophysical Journal* 863.1, 88 (Aug. 2018), p. 88. DOI: 10.3847/1538-4357/aacf9d. arXiv: 1807.05231 [astro-ph.GA].

[17] Nagayoshi Ohashi, Masahiko Hayashi, Paul T. P. Ho, and Munetake Momose. "Interferometric Imaging of IRAS 04368+2557 in the L1527 Molecular Cloud Core: A Dynamically Infalling Envelope with Rotation." In: *The Astrophysical Journal* 475.1 (Jan. 1997), pp. 211–223. DOI: 10.1086/303533.

[18] Nami Sakai, Takeshi Sakai, and Satoshi Yamamoto. "Tentative Detection of C4H-toward the Low-Mass Protostar IRAS 04368+2557 in L1527." In: *The Astrophysical Journal* 673.1 (2007), pp. L71–L74. DOI: 10.1086/527376. URL: https://doi.org/10.1086%2F527376.

[19] Nami Sakai, Takeshi Sakai, Tomoya Hirota, and Satoshi Yamamoto. "Abundant Carbon-Chain Molecules toward the Low-Mass Protostar IRAS 043682557 in L1527." In: *The Astrophysical Journal* 672.1 (Jan. 2008), pp. 371–381. DOI: 10.1086/523635. URL: https://doi.org/10.1086%2F523635.

[20] F. H. Shu. "Self-similar collapse of isothermal spheres and star formation." In: *The Astrophysical Journal* 214 (June 1977), pp. 488–497. DOI: 10.1086/155274.

[21] L. Spitzer. *Physical processes in the interstellar medium*. 1978. DOI: 10.1002/9783527617722.

[22] S. Terebey, C. J. Chandler, and P. Andre. "The Contribution of Disks and Envelopes to the Millimeter Continuum Emission from Very Young Low-Mass Stars." In: *The Astrophysical Journal* 414 (Sept. 1993), p. 759. DOI: 10.1086/173121.

[23] John J. Tobin, Lee Hartmann, Hsin-Fang Chiang, David J. Wilner, Leslie W. Looney, Laurent Loinard, Nuria Calvet, and Paola D'Alessio. "A ~0.2-solar-mass protostar with a Keplerian disk in the very young L1527 IRS system." In: *Nature* 492.7427 (Dec. 2012), pp. 83–85. DOI: 10.1038/nature11610. arXiv: 1212.0861 [astro-ph.GA].

[24] Wu, Yuefang et al. "A particular carbon-chain-producing region: L1489 starless core." In: *A&A* 627 (2019), A162. DOI: 10.1051/0004-6361/201834184. URL: https://doi.org/10.1051/0004-6361/201834184.

[25] Hsi-Wei Yen et al. "ALMA Observations of Infalling Flows toward the Keplerian Disk around the Class I Protostar L1489 IRS." In: *The Astrophysical Journal* 793.1, 1 (Sept. 2014), p. 1. DOI: 10.1088/0004-637X/793/1/1. arXiv: 1407.2699 [astro-ph.SR].

APPENDIX

5.7 BRIGHTNESS TEMPERATURE

The conversion from Jy/beam to Kelvin was done as follows.

The brightness temperature is given by

$$T = \frac{\lambda^2}{2k\Omega} S \tag{1}$$

Where Ω is the beam solid angle and S the flux density.

$$\Omega = \frac{\pi\theta_{maj}\theta_{min}}{4 \ln 2}$$

[For the beamwidth, the Half Power Beam Width (HPBW) is used. Which is equivalent to the Full Width Half Maximum (FWHM) in one dimension.]

$$\frac{S}{\Omega} = I \frac{beam}{\Omega} \tag{2}$$

So equation 1 becomes

$$T = 1.222 \cdot 10^3 \frac{I}{\nu^2} \theta_{maj}\theta_{min} \tag{3}$$

5.8 QUANTUM NUMBERS

Notation: (551 542) means N=5-5, J=5-4, I=1-2, where N is the principal quantum number, J is the angular momentum.